

## Enhanced performance of resonant sub-terahertz detection in a plasmonic cavity

G. C. Dyer,<sup>1,a)</sup> S. Preu,<sup>2</sup> G. R. Aizin,<sup>3</sup> J. Mikalopas,<sup>3</sup> A. D. Grine,<sup>1</sup> J. L. Reno,<sup>1</sup> J. M. Hensley,<sup>4</sup> N. Q. Vinh,<sup>2</sup> A. C. Gossard,<sup>2</sup> M. S. Sherwin,<sup>2</sup> S. J. Allen,<sup>2</sup> and E. A. Shaner<sup>1</sup>

<sup>1</sup>Sandia National Laboratories, P.O. Box 5800, Albuquerque, New Mexico 87185, USA

<sup>2</sup>Institute for Terahertz Science and Technology, UC Santa Barbara, Santa Barbara, California 93106, USA

<sup>3</sup>Kingsborough College, The City University of New York, Brooklyn, New York 11235, USA

<sup>4</sup>Physical Sciences Inc., Andover, Massachusetts 01810, USA

(Received 3 October 2011; accepted 3 February 2012; published online 23 February 2012)

A multi-gate high electron mobility transistor coupled to a log-periodic antenna was engineered to detect sub-terahertz radiation through resonant excitation of plasmon modes in the channel. The device was integrated with a silicon hyper-hemispherical lens in order to enhance radiation collection and eliminate parasitic substrate modes. The continuous detector response spectrum from 185 GHz to 380 GHz indicates the presence of distinct collective plasmonic cavity modes resulting from the quantization of the plasmon wavevector. In a bolometric detection mode, a noise equivalent power of less than 50 pW/Hz<sup>1/2</sup> and a responsivity exceeding 100 kV/W have been measured at 11.5 K. © 2012 American Institute of Physics. [doi:10.1063/1.3687698]

The field of terahertz (THz) science has witnessed a rapid evolution in the last decade as source and detector technologies have been developed in attempts to fill the so-called “THz gap” of the electromagnetic spectrum. Cryogenically cooled bolometers are utilized as THz detectors for applications requiring extremely high sensitivity,<sup>1–3</sup> while Schottky diodes have been preferred for room temperature detection.<sup>4</sup> Plasmonic field effect transistors (FETs) have shown perhaps the greatest versatility because plasma waves generated in a transistor channel may be applied to both non-resonant and resonant detection applications,<sup>5–12</sup> as well as to heterodyne mixing.<sup>13,14</sup> If adequate sensitivity could be attained, detectors based on high electron mobility transistors (HEMTs) are especially well-suited to applications requiring tunable resonant detection. Here, coupling of a THz field to two-dimension plasmons excited in the transistor channel can be facilitated by either a grating<sup>15–19</sup> or an antenna.<sup>20–22</sup> In this letter, we report several developments in the performance of the tuned plasmonic detectors described in Refs. 21 and 22. These devices feature a micron scale multi-gate HEMT placed at the vertex of a broadband antenna. The integration of a Si lens has enhanced detector performance by an additional order of magnitude while also enabling high resolution characterization of the detector response spectrum.

The sub-THz detector shown in Fig. 1(a) is designed to integrate three fundamental components: a resonant 2D plasmonic absorber, a bolometric detection element, and a coupling mechanism to address the momentum mismatch between radiation in free space and in 2D plasmons. In this scheme, the channel of a HEMT fabricated at the antenna vertex functions as a resonant absorber. The HEMT channel is 14 μm long by 10 μm wide, with the source, drain, and gate terminals defining the fundamental wavevector of a 2D plasmon excitation. Three 2 μm wide gates spaced from

neighboring terminals and each other by 2 μm are used to control the carrier density and, thus, tune plasmon resonances. The HEMT is fabricated from a double quantum well GaAs/AlGaAs heterostructure (Sandia wafer EA1149) with a total electron density of  $4.14 \times 10^{11} \text{ cm}^{-2}$ , a mobility of over  $10^6 \text{ cm}^2/\text{V s}$  at liquid He temperature, and channel pinch off voltage of  $V_{\text{TH}} = -2.4 \text{ V}$  at 11.5 K. The quantum wells are 400 nm below the surface, 20 nm thick, and spaced 7 nm from each other. One gate, labeled BG for bolometric gate, is biased beyond threshold to create a region of thermally activated transport.<sup>23</sup> This style of multi-section gating with an integrated bolometric region has been shown in past work to enhance the sensitivity of larger grating-gate style devices while maintaining tunability.<sup>18</sup>

A self-complementary log-periodic antenna with  $R_{\text{rad}} \cong 60\pi\sqrt{2}/(\epsilon_{\text{GaAs}} + 1) \cong 72 \Omega$  on a GaAs substrate provides broadband coupling of the THz field to the source and drain terminals of the HEMT.<sup>24–27</sup> The detector chip is mounted on a 1 cm diameter Si hyper-hemispherical lens as shown in Fig. 1(b), and incident radiation is coupled through the substrate. For  $f/l$  optics, the diffraction-limited Gaussian beam waist exceeds the effective cross section of a log-periodic antenna. Lens coupling through the substrate enhances the field intensity at the effective antenna cross section across its

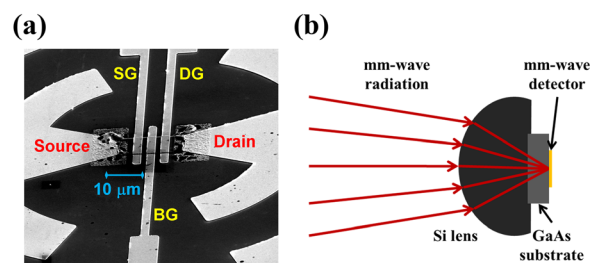


FIG. 1. (Color online) (a) Micrograph of a 10 μm wide by 14 μm long HEMT with three independently biased gates at the vertex of a broadband antenna. (b) Mounting of the detector with a Si hyper-hemispherical lens is shown. The detector is illuminated through the substrate.

<sup>a)</sup>Author to whom correspondence should be addressed. Electronic mail: gcdyer@sandia.gov.

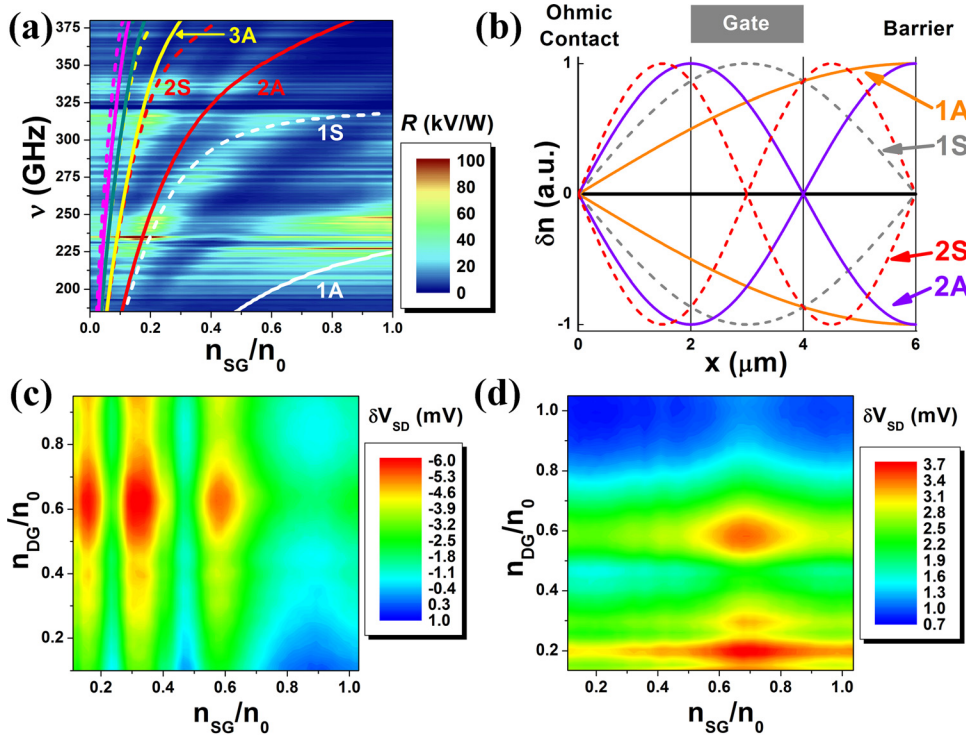


FIG. 2. (Color online) (a) The detector response is mapped as a function of excitation frequency  $\nu$  and normalized carrier density  $n_{SG}/n_0$  under SG. Theoretically derived modes are plotted in solid and dashed lines. Solid lines correspond to A boundary conditions, while dashed lines correspond to S boundary conditions. Mode number and type are indicated for the first five modes. (b) The normalized carrier density modulation for the first four modes, labeled by number and type, is shown with  $n_{SG}/n_0 = 1$ . (c) The detector voltage signal with 370 GHz excitation and  $I_{SD} = +500$  nA is plotted as a function of  $n_{SG}/n_0$  and  $n_{DG}/n_0$ . (d) The detector voltage signal with 370 GHz excitation and  $I_{SD} = -500$  nA is plotted as a function of both  $n_{SG}/n_0$  and  $n_{DG}/n_0$ .

operating bandwidth relative to direct coupling from free space to antenna. The integrated lens has an important additional function in that by removing a specular surface, Fabry-Perot modes in the substrate are significantly mitigated due to the close index match of GaAs and Si.

The detector responsivity as a function of frequency and source gate (SG) bias has been measured when illuminated by a tunable set of Virginia Diodes Schottky multipliers, upconverting a fundamental signal from a vector network analyzer (Fig. 2). The multi-gate transistor was cooled to 11.5 K to maximize the bolometric response. The bolometric gate, labeled BG in Fig. 1(a), was biased beyond threshold,  $V_{BG} = -2.7$  V, and source-drain current was set to  $I_{SD} = +500$  nA such that electrons were drifting from source towards the bolometric region. The SG bias was tuned from  $+0.3$  V to  $-2.7$  V. The normalized carrier density under the source gate is given by  $n_{SG}/n_0 = (V_{TH} - V_{SG})/V_{TH}$  assuming a simple capacitive relationship between gate voltage and carrier density, where  $V_{TH}$  is the threshold voltage. The continuous wave source was mechanically chopped at 320 Hz, and the RMS amplitude of the first harmonic of the approximately square wave detector signal  $\delta V_{SD}^{RMS}$  was measured with a lock-in amplifier. The detector responsivity  $R = 2\sqrt{2}A_1^{-1}\delta V_{SD}^{RMS}/P$  has been calculated to reflect the full peak-peak square wave signal. Here,  $A_1 = 4/\pi$  is the coefficient of the first Fourier term of a square waveform. The incident power,  $P$ , is measured before the cryostat window with no scaling for detector dimensions, correction for window losses or reflectivity from the lens. A continuous spectrum of 2D plasmonic modes from 185 GHz to 380 GHz is evident. Alternating bands of high and low responsivity spaced by approximately 5 GHz are likely due to Fabry-Perot resonances introduced by specular surfaces along the beam path.

Based on the hydrodynamic model together with the Poisson equation for a 2DEG developed in Ref. 21, the eight

lowest order modes for a  $6\ \mu\text{m}$  2D plasma cavity with a  $2\ \mu\text{m}$  gated stripe in its center between SG and BG in Fig. 1(a) have been calculated for two different sets of boundary conditions.<sup>5,6</sup> The hydrodynamic model eigenmodes are determined solely from intrinsic material parameters, device geometry, and fundamental constants. The results are plotted in Fig. 2(a) as lines where the mode number  $m$  and the mode type are indicated for the first five modes. The solid lines correspond to eigenmodes with asymmetric (A) boundary conditions: zero 2D density fluctuation  $\delta n = 0$  at the source contact and zero fluctuation of current  $\delta I = n_0\delta v = 0$  at the depleted region under the bolometric gate. The dashed lines correspond to eigenmodes with symmetric (s) boundary conditions: zero 2D density fluctuation  $\delta n = 0$  at both source contact and depleted barrier region. The hydrodynamic model eigenmodes in Fig. 2(a) must be considered in the context of the complete device formed by antenna, bolometric sensor, and 2D plasma cavities.<sup>28</sup> The 2D plasmon is excited by the injection of THz current at an Ohmic contact. The electric field across the antenna structure drives a current to its vertex, while the Ohmic contacts and surrounding metallization damp and shunt any charge fluctuation that could accumulate at the source (or drain) terminal. The carrier density fluctuation in the cavity is consequently a node ( $\delta n = 0$ ) at the Ohmic contact. The resonant cavity modes are then determined by the boundary conditions at the opposite side of the cavity where the barrier gate has fully depleted the 2DEG. A node in either carrier density or velocity fluctuation at the barrier then satisfies the resonance condition. The respective asymmetric and symmetric eigenmodes, illustrated in Fig. 2(b) with  $n_{SG}/n_0 = 1$ , should be considered only as upper and lower bounds of the measured eigenmodes. At large electron density modulations,  $n_{SG}/n_0 \rightarrow 0$ , the plasma modes are increasingly localized under the low electron density gated region. They become less sensitive to the

boundary conditions at the cavity ends since the wavevector of the 2D plasma resonance is now determined by the size of the gated region only.<sup>21</sup> Therefore, in this limit, the calculated  $m$ th symmetric and  $m+1$ th asymmetric modes approach each other and merge. The calculated plasma frequencies are in very good quantitative agreement with the measured ones in Fig. 2(a) in this limit. However, the highest order modes cannot be resolved experimentally due to damping broadening the resonances.

The overall behavior of the calculated and measured modes as a function of electron density and the measured and calculated resonant frequencies is in good semi-quantitative agreement. However, at this stage, the model cannot be considered as a fit to the data since the antenna-detector circuit effects as well as resistive damping are not included into the model. Though in Fig. 2(a), the drain cavity between the BG and drain terminal is not tuned, a series of resonances is excited in this cavity as frequency is swept. The frequency-dependent excitation of the drain cavity introduces additional structure to the bolometric response spectrum.

The effect of mutual resonances in both source and drain cavity is evidenced more clearly in Figs. 2(c) and 2(d). Here, both cavities are tuned independently with 370 GHz radiation incident, where the normalized carrier density below the drain gate (DG) defined as  $n_{DG}/n_0 = (V_{TH} - V_{DG})/V_{TH}$ . The bolometric mechanism is highly sensitive to polarity of current.<sup>18,21</sup> Positive bias of  $I_{SD} = +500$  nA, with majority carriers drifting from source to drain, produces a decrease in source-drain voltage on resonance primarily due to plasmon resonant heating in the source cavity. Under positive bias, the resonances appear as vertical bands in Fig. 2(c). Negative bias of  $I_{SD} = -500$  nA, with majority carriers drifting from drain to source, produces the reciprocal effect: an increase in source-drain voltage on resonance primarily due to plasmon resonant heating in the drain cavity. Under negative bias, the resonances appear as horizontal bands in Fig. 2(d). These results are consistent with resonant absorption lowering DC resistance of the barrier region.

The non-uniform amplitude of the resonances in Figs. 2(c) and 2(d) indicates that the two cavities are not fully independent. The resonant detector response associated with either cavity shows a marked increase in signal amplitude when resonant conditions in the neighboring cavity are also met. This effect is most pronounced when resonant features in one cavity intersect the lowest order resonance in another cavity at normalized electron density around  $n/n_0 \sim .6$ . The lack of repelled crossings in this data indicates this is not a coherent effect. Rather, the coupling mechanism, whether mediated through shared bolometric heating or through the modification of the coupling of the external THz field to the individual plasma cavities, is incoherent. The nature of this shared contribution to the bolometric signal is not fully understood at this time.

The noise equivalent power (NEP) as a function of modulation frequency is shown in Fig. 3(a) for 100 nA, 300 nA, and 500 nA source-drain bias currents. The excitation frequency is 241 GHz where the detector shows a strong resonant response with DG and SG set to zero bias. Responsivity was measured using a Stanford Research 830 lock-in amplifier with the detector operated at 11.5 K and  $V_{BG} = -2.834$  V.

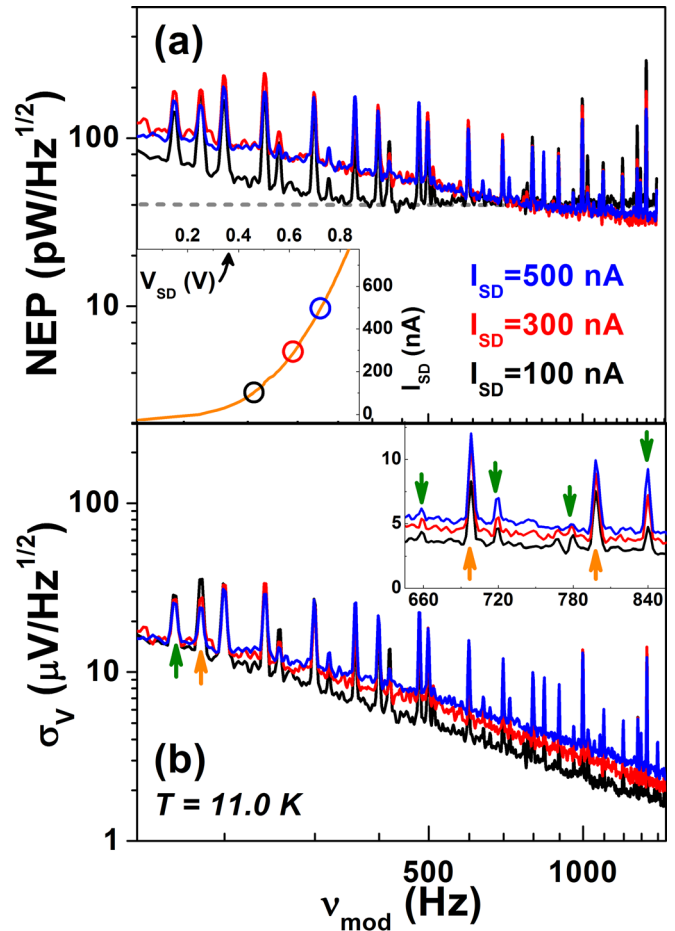


FIG. 3. (Color online) (a) The detector NEP as modulation frequency is swept with 241 GHz excitation for 100 nA, 300 nA, and 500 nA source-drain bias currents. The detector was operated at 11.5 K for responsivity measurements and 11.0 K for noise density spectrum characterization. The inset shows the detector I-V in the positive quadrant with the bias points, where NEP is calculated, highlighted by their respective colors. (b) The detector noise density spectrum at 11.0 K with  $V_{BG} = -2.450$  V. The inset highlights the harmonics of environmental noise sources at 60 Hz and 100 Hz.

Responsivity  $R = 2/\sqrt{2}\delta V_{SD}^{RMS}/P$  was calculated from the peak-peak detector signal because the waveform is not constant with fixed Fourier decomposition over a broad range of modulation frequencies. The detector responsivity exceeds 100  $\text{kV/W}$  for all three bias currents measured with the modulation frequency set below 400 Hz. A second sample of identical design and material was characterized with a Stanford Research 785 RF Spectrum Analyzer in a He flow cryostat optimized to minimize experimental noise sources. At optimal combinations of source-drain current bias and modulation frequency, the NEP approaches 40  $\text{pW/Hz}^{1/2}$ , while typical results are between 50 and 100  $\text{pW/Hz}^{1/2}$ . Only spectrally narrow experimental sources such as power line noise at 60 Hz and an environmental source at 100 Hz plus harmonics thereof highlighted in the inset of Fig. 3(b) obscure the intrinsic detector electronic noise. The detector was operated at 11.0 K and  $V_{BG} = -2.450$  V for the noise measurements to replicate source-drain I-V characteristics where responsivity was measured. Persistent drift of the barrier operating point, as large as 500–600 mV, over a duration of several hours required re-tuning of the bolometric gate to achieve an identical operating point. Responsivity measurements were performed after

barrier operating point had drifted several hundred mV from its initial threshold value near  $-2.400$  V.

The trending behavior of the NEP is a combination of the simultaneous roll-off of both noise density and detector responsivity with increased modulation frequency. At sufficiently large modulation frequency, a  $1/f$  dependence is evident in both responsivity and noise spectra, thus the NEP reaches a nearly flat minimum. Fitting the lower envelope of the noise voltage spectra in Fig. 3(b) to a filter roll-off yields circuit time constants of 2.7 ms, 1.6 ms, and 1.1 ms for 100 nA, 300 nA, and 500 nA bias points, respectively. The differential resistances for the respective bias points calculated from the I-V in the inset of Fig. 3(a) is 1.11 M $\Omega$ , 0.61 M $\Omega$ , and 0.45 M $\Omega$ . The response time tracks the differential resistance, consistent with prior study of bolometric detection in multi-gate HEMTs where the response time is a circuit time constant.<sup>23</sup>

The results presented in this letter are an important step towards on-chip spectroscopic sub-THz and THz detection. We have demonstrated an enhancement in responsivity of over an order of magnitude relative to a detector without an integrated Si lens.<sup>21</sup> This is consistent with the expected improvement from matching of the beam waist to the effective antenna cross section. A complicated but tractable harmonic spectrum of 2D plasmonic resonances has emerged from characterization of the detector as a continuous function of both excitation frequency and gate bias. The combination of a low NEP with 2D plasmonic resonances that can be engineered across the THz spectrum provides potential opportunities for electronically tunable spectroscopy in the THz band. Scaling the fundamental plasma frequency upward by reducing the size of devices is of particular interest for future study.

This work is supported by the University of Buffalo NSF-NIRT THz Collaboratory: ECS0609146. This work was performed, in part, at the Center for Integrated Nanotechnologies, a U.S. Department of Energy, Office of Basic Energy Sciences user facility. Sandia National Laboratories is a multi-program laboratory managed and operated by Sandia Corporation, a wholly owned subsidiary of Lockheed Martin Corporation, for the U.S. Department of Energy's National Nuclear Security Administration under contract DE-AC04-94AL85000. This material is based upon work supported by the U.S. Air Force Office of Scientific Research, Arlington, VA, under Contract No. FA9550-10-C-0172 and Physical Sciences Inc. Andover, MA, under Agreement No. FI011090528. Any opinions, findings, and conclusions or recommendations expressed in this material are those of the author(s) and do not necessarily

reflect the views of the U.S. AFOSR or Physical Sciences Inc. S.P. also acknowledges the Humboldt foundation and the NSF MRSEC program DMR-0520415 (MRL-UCSB) for funding.

- <sup>1</sup>S. Komiyama, O. Astafiev, V. Antonov, T. Kutsuwa, and H. Hirai, *Nature* **403**, 405 (2000).
- <sup>2</sup>P. K. Day, H. G. LeDuc, B. A. Mazin, A. Vayonakis, and J. Zmuidzinas, *Nature* **425**, 817 (2003).
- <sup>3</sup>B. S. Karasik and R. Cantor, *Appl. Phys. Lett.* **98**, 193503 (2011).
- <sup>4</sup>E. R. Brown, A. C. Young, J. Zimmerman, H. Kazemi, and A. C. Gossard, *IEEE Microw. Mag.* **8**, 54 (2007).
- <sup>5</sup>M. I. Dyakonov and M. S. Shur, *Phys. Rev. Lett.* **71**, 2465 (1993).
- <sup>6</sup>M. I. Dyakonov and M. S. Shur, *Appl. Phys. Lett.* **87**, 111501 (2005).
- <sup>7</sup>M. I. Dyakonov and M. S. Shur, *IEEE Trans. Electron Devices* **43**, 380 (1996).
- <sup>8</sup>W. Knap, M. I. Dyakonov, D. Coquillat, F. Teppe, N. Dyakonova, J. Łusakowski, K. Karpierz, M. Sakowicz, G. Valusis, D. Seliuta *et al.*, *J. Infrared Milli. Terahz. Waves* **30**, 1319 (2009).
- <sup>9</sup>A. Lisauskas, U. R. Pfeiffer, E. Öjefors, P. H. Bolivar, D. Glaab, and H. G. Roskos, *J. Appl. Phys.* **105**, 114511 (2009).
- <sup>10</sup>S. J. Allen, D. C. Tsui, and R. A. Logan, *Phys. Rev. Lett.* **38**, 980 (1977).
- <sup>11</sup>T. A. Elkhatib, V. Yu. Kachorovskii, W. J. Stillman, S. Rumyantsev, X. C. Zhang, and M. S. Shur, *Appl. Phys. Lett.* **98**, 243505 (2011).
- <sup>12</sup>S. Kim, J. D. Zimmerman, P. Focardi, A. C. Gossard, D. H. Wu, and M. S. Sherwin, *Appl. Phys. Lett.* **92**, 253508 (2008).
- <sup>13</sup>D. Glaab, S. Boppel, A. Lisauskas, U. R. Pfeiffer, E. Öjefors, and H. G. Roskos, *Appl. Phys. Lett.* **96**, 042106 (2010).
- <sup>14</sup>M. Lee, M. C. Wanke, and J. L. Reno, *Appl. Phys. Lett.* **86**, 033501 (2005).
- <sup>15</sup>V. V. Popov, O. V. Polischuk, T. V. Teperik, X. G. Peralta, S. J. Allen, N. J. M. Horing, and M. C. Wanke, *J. Appl. Phys.* **94**, 3556 (2003).
- <sup>16</sup>E. A. Shaner, M. Lee, M. C. Wanke, A. D. Grine, J. L. Reno, and S. J. Allen, *Appl. Phys. Lett.* **87**, 193507 (2005).
- <sup>17</sup>E. A. Shaner, M. C. Wanke, M. Lee, J. L. Reno, S. J. Allen, and X. G. Peralta, *Proc. SPIE* **5790**, 116 (2005).
- <sup>18</sup>E. A. Shaner, A. D. Grine, M. C. Wanke, M. Lee, J. L. Reno, and S. J. Allen, *IEEE Photon. Technol. Lett.* **18**, 1925 (2006).
- <sup>19</sup>V. V. Popov, D. M. Ermolaev, K. V. Maremyanin, N. A. Maleev, V. E. Zemlyakov, V. I. Gavrilenko, and S. Yu. Shapoval, *Appl. Phys. Lett.* **98**, 153504 (2011).
- <sup>20</sup>V. Ryzhii, A. Satou, T. Otsuji, and M. S. Shur, *J. Appl. Phys.* **103**, 014504 (2008).
- <sup>21</sup>G. C. Dyer, N. Q. Vinh, S. J. Allen, G. R. Aizin, J. Mikalopas, J. L. Reno, and E. A. Shaner, *Appl. Phys. Lett.* **97**, 193507 (2010).
- <sup>22</sup>G. C. Dyer, G. R. Aizin, J. L. Reno, E. A. Shaner, and S. J. Allen, *IEEE J. Sel. Top. Quantum Electron.* **17**, 85 (2011).
- <sup>23</sup>G. C. Dyer, J. D. Crossno, G. R. Aizin, E. A. Shaner, M. C. Wanke, J. L. Reno, and S. J. Allen, *J. Phys.: Condens. Matter* **21**, 195803 (2009).
- <sup>24</sup>K. A. McIntosh, E. R. Brown, K. B. Nichols, O. B. McMahon, W. F. DiNatale, and T. M. Lyszczarz, *Appl. Phys. Lett.* **69**, 3632 (1996).
- <sup>25</sup>E. R. Brown, A. W. M. Lee, B. S. Navi, and J. E. Bjarnason, *Microwave Opt. Technol. Lett.* **48**, 524 (2006).
- <sup>26</sup>G. M. Rebeiz, W. G. Regehr, D. B. Rutledge, R. L. Savage, and N. C. Luhmann, *Int. J. Infrared Millim. Waves* **8**, 1249 (1987).
- <sup>27</sup>R. H. DuHamel and D. E. Isbell, *IRE Int. Conv. Rec.* Part I, 119 (1957).
- <sup>28</sup>P. J. Burke, I. B. Spielman, J. P. Eisenstein, L. N. Pfeiffer, and K. W. West, *Appl. Phys. Lett.* **76**, 745 (2000).